Nanostructured Ti–Zr–Pd–Si–(Nb) bulk metallic composites: novel biocompatible materials with superior mechanical strength and elastic recovery

Journal:	*Journal of Biomedical Materials Research: Part B - Applied Biomaterials*
Manuscript ID:	JBMR-B-14-0409.R1
Wiley - Manuscript type:	Original Research Report
Date Submitted by the Author:	n/a
Complete List of Authors:	Hynowska, Anna; Universitat Autònoma de Barcelona , Physics Blanquer, Andreu; Universitat Autònoma de Barcelona, Departament de Biologia Cel•lular, Fisiologia i Immunologia Pellicer, Eva; Universitat Autònoma de Barcelona, Departament de Física Fornell, Jordina; Universitat Autònoma de Barcelona, Departament de Física Suriñach, Santiago; Universitat Autònoma de Barcelona, Departament de Física Baró, Maria; Universitat Autonoma de Barcelona, Dep. Fisica Gebert, Annett; IFW, institute for metallic materials Calin, Mariana; Leibniz-Institute for Solid State and Materials Research IFW Dresden, Institute for Complex Materials Eckert, Jürgen Nogués, Carme; Universitat Autonoma de Barcelona, Departament de Biologia Cel·lular, Fisiologia i Immunologia Ibáñez, Elena; Universitat Autonoma de Barcelona, Departament de Biologia Cel·lular, Fisiologia i Immunologia Barrios, Lleonard; Universitat Autonoma de Barcelona, Departament de Biologia Cel·lular, Fisiologia i Immunologia Sort, Jordi; Universitat Autonoma de Barcelona, Física
Keywords:	titanium (alloys), Nanomaterials/nanophase, mechanical properties, biocompatibility/hard tissue

Nanostructured Ti-Zr-Pd-Si-(Nb) bulk metallic composites: novel biocompatible materials with superior mechanical strength and elastic recovery

A. Hynowska[1], A. Blanquer[2], E. Pellicer[1,*], J. Fornell[1], S. Suriñach[1], M. D. Baró[1], A. Gebert[3], M. Calin[3], J. Eckert[3,4], C. Nogués[2], E. Ibáñez[2], L. Barrios[2,§], J. Sort[5]

[1]Departament de Física, Universitat Autònoma de Barcelona, E-08193 Bellaterra, Spain
[2]Departament de Biologia Cel·lular, Fisiologia i Immunologia, Universitat Autònoma de Barcelona, E-08193 Bellaterra, Spain
[3]IFW Dresden, P.O. Box 270116, D-01171 Dresden, Germany
[4]TU Dresden, Institute of Materials Science, D-01062 Dresden, Germany
[5]Institució Catalana de Recerca i Estudis Avançats (ICREA) and Departament de Física, Universitat Autònoma de Barcelona, E-08193 Bellaterra, Spain

* To whom correspondence should be addressed: *Eva.Pellicer@uab.cat,
§Lleonard.Barrios@uab.cat

Tel.: +34 935811401; +Fax: +34 935812155.

1

Abstract: The microstructure, mechanical behaviour and biocompatibility (cell culture, morphology and cell adhesion) of nanostructured $Ti_{45}Zr_{15}Pd_{35-x}Si_5Nb_x$ with x = 0, 5 (at. %) alloys, synthesized by arc melting and subsequent Cu mould suction casting, in the form of rods with 3 mm in diameter, are investigated. Both Ti-Zr-Pd-Si-(Nb) materials show a multi-phase (composite-like) microstructure. The main phase is cubic β-Ti phase (Im3m) but hexagonal α-Ti (P63/mmc), cubic TiPd (Pm3m), cubic PdZr (Fm3m), and hexagonal $(Ti,Zr)_5Si_3$ (P63/mcm) phases are also present. Nanoindentation experiments show that the $Ti_{45}Zr_{15}Pd_{30}Si_5Nb_5$ sample exhibits lower Young's modulus than $Ti_{45}Zr_{15}Pd_{35}Si_5$. Conversely, $Ti_{45}Zr_{15}Pd_{35}Si_5$ is mechanically harder. Actually, both alloys exhibit larger values of hardness when compared to commercial Ti-40Nb, ($H_{Ti-Zr-Pd-Si} \approx 14$ GPa, $H_{Ti-Zr-Pd-Si-Nb} \approx 10$ GPa and $H_{Ti-40Nb} \approx 2.7$ GPa). Concerning the biological behaviour, preliminary results of cell viability performed on several Ti-Zr-Pd-Si-(Nb) discs indicate that the number of live cells is superior to 94% in both cases. The studied Ti-Zr-Pd-Si-(Nb) bulk metallic system is thus interesting for biomedical applications because of the outstanding mechanical properties (relatively low Young's modulus combined with large hardness), together with the excellent biocompatibility.

Keywords: Bioimplant, Ti-based alloy, nanostructured material, mechanical behaviour, biological tests.

INTRODUCTION

Due to the fast population aging, a concern related to the development of suitable materials for bone replacement is continuously arising.[1,2] Specifically, the aim of current investigations is to develop orthopaedic implants that can stand for longer periods of time or even the entire lifetime

without failure or need for a revision surgery.[3] These orthopaedic implants must therefore show bio- and mechanical-compatibility with bone. The ideal implant material should not cause any foreign-body inflammatory response, the growth of microorganisms should be suppressed, and it should be non-toxic, non-allergenic and non-carcinogenic.[4] From the mechanical point of view, there are several issues having an impact on the selection of suitable permanent biomaterials. Namely, the candidate material must possess high strength, high hardness, high elastic strain limit, and relatively low Young's modulus to avoid the occurrence of the so-called stress shielding effect.[5-7] This phenomenon, which occurs when the Young's modulus of the permanent implant differs significantly from the Young's modulus of bone, can ultimately lead to implant loosening. Traditionally, 316L austenitic steel, Co–Cr and Ti alloys have been employed in the biomedical field.[6] Thus, Ti and its alloys have become the most promising engineering materials because they combine high strength with relatively low Young's modulus, reduced stiffness and rather low density (4.5 g/cm^3). In addition, they show good biocompatibility and good corrosion resistance, in many cases superior to those of conventional steel and Co-Cr alloys.[8] So far, the mostly used Ti-based alloys are Ti-6Al-4V (composed of α and β phases) and Ti-40Nb (composed of β phase).[1,5,9-11] Both materials have found applications in many medical devices as biomaterials for orthopaedic implants because of their outstanding mechanical properties.[3] Nevertheless, these alloys face some undesired and unsolved problems. Ti-6Al-4V contains aluminium, which is known to cause certain bone diseases and neurological disorders.[13] and vanadium may become toxic at excessive concentration levels. The toxicity of vanadium is well-known, and can be exacerbated if the implant fractures and undergoes subsequently fretting.[4] Another major concern of Ti-6Al-4V is the mismatch between its Young's modulus (E = 110 – 120 GPa) and that of bone (E = 10 – 30 GPa)[14] that, as aforementioned, can cause implant

3

failure.[15] In spite of the exceedingly low stiffness, Ti-40Nb shows good biocompatibility and possesses lower Young's modulus.[15-19] Therefore, it is of outmost importance to further search for novel bulk Ti-based materials which satisfy: (*i*) chemical composition containing neither toxic nor allergenic elements, and (*ii*) suitable microstructures that promote the targeted mechanical properties. In recent years, bulk metallic glassy alloys based on titanium have been developed.[20-24] The progress in the design of bulk metallic glasses has also led to progress in the development of new in situ formed nano-scale structured materials, which may exhibit even better mechanical performance than bulk metallic glasses (BMGs) and/or traditional commercial Ti-based alloys.[25,26] Although it is known that BMGs exhibit high strength and large elastic strain, they usually fail catastrophically by the fast propagation of shear bands, leaving zero global plastic strain under tension. Therefore, second phase particles are in-situ or ex-situ introduced to reinforce the metallic glass matrices and arrest the shear bands, leading to bulk metallic glass composites.[27] In turn, composites made of nanocrystalline phases can exhibit very large hardness (due to dislocation pile-up at grain boundaries) and high plasticity (particularly when additional deformation mechanisms are activated such as intergranular grain boundary sliding).[28] This has triggered the interest in nanostructured bulk metallic composites in several fields like biomaterials, aerospace industry and other structural applications. Considering the biomedical applications, we have focused on the development of new nano/ultrafine-structured Ti-based alloys free of any toxic or allergic elements (e.g. Ni, Cu, Al, V, etc.) and succeeded in finding compositions with superior mechanical properties. Here, the synthesis and characterization of a new Ti-based alloy composition (i.e., $Ti_{45}Zr_{15}Pd_{35-x}Si_5Nb_x$ with x = 0 and 5 at. %) in bulk form is reported. This particular composition (without Nb) had been previously synthesised in the form of melt-spun amorphous ribbons but not in bulk.[29] According to Oak et al. and Inoue, this alloy has the potential to be applied in the biomedical field as an orthopaedic bone fixation device.[29] In

4

our work, niobium was chosen to partially replace palladium for several reasons. First of all, Nb is much cheaper than Pd and it is a well-known non-toxic and non-allergic element.[30] Besides, addition of Nb promotes the formation of β-phase because it belongs to the β-stabilizer elements.[31] In general, an increase in the amount of β-phase causes a decrease of the Young's modulus, an improvement of the alloy formability and an enhancement of the corrosion resistance.[32] Indeed, β-Ti alloys are better suited for biomedical applications than α-Ti alloys. Finally, it has been reported that Nb can be alloyed to Ti in order to reduce the Young's modulus without compromising the strength.[33,34] Our results reveal that the addition of Nb to $Ti_{45}Zr_{15}Pd_{35-x}Si_5$ brings about a reduction of Young's modulus while preserving reasonably high strength values and not causing detrimental effects on the alloy biocompatibility.

MATERIALS AND METHODS

Master alloys with composition $Ti_{45}Zr_{15}Pd_{35-x}Si_5Nb_x$ (where x = 0 and 5 at. %) were prepared by arc melting a mixture of the highly pure elements (> 99.99% wt. %) under a Ti-gettered Ar atmosphere on a water cooled Cu heart. Rods of 3 mm in diameter were obtained from the melt by suction casting into a Cu mould. The microstructures of as-cast samples were examined using a scanning electron microscope (SEM Zeiss Merlin), equipped with an energy dispersive X-ray detector (EDX, Oxford Instruments, INCA system). The samples were structurally characterised by X-ray diffraction (XRD) (Philips X'Pert diffractometer with monochromatic Cu-K_α radiation). MAUD (Material Analysis Using Diffraction) software based on the Rietveld method was applied to calculate lattice parameters and phase percentages from powder XRD. Transmission electron microscopy (TEM) (JEOL JEM 2011, 200 kV) was used for microstructure observations. Samples for TEM imaging were mechanically pre-thinned to 80 μm and afterwards

5

the thickness was reduced to 30 μm by mechanical dimpling at one side of the samples. Finally, further thinning of the disks was carried out by ion beam milling at 4 keV at an incident angle of 5°. The elastic properties were evaluated by ultrasonic measurements (pulse-echo overlap technique) along with density assessment (Archimedes' method). The mechanical properties of the as-cast Ti-Zr-Pd-Si-(Nb) alloys were determined by nanoindentation measurements using UMIS equipment from Fischer-Cripps laboratories,[35] equipped with a Berkovich pyramidal-shaped indenter tip. The thermal drift was always kept below $\pm$ 0.05 nm s^{-1}. Arrays of 50 and 100 indentations with maximum applied loads of 250 mN and 3 mN, respectively, were carried out to probe both the average and local mechanical behaviour of the samples and to verify the accuracy of the indentation data. Prior to the nanoindentation tests, the specimens were carefully polished to mirror-like appearance using diamond paste. The method of Oliver and Pharr was used to determine the hardness and the reduced Young's modulus.[36] Finally, the elastic/total indentation energies were also calculated. The total mechanical work done by the indenter during loading, U_{tot}, was calculated from the area enclosed between the loading indentation segment and the displacement axis. This energy is the sum of the elastic, U_{el}, and the plastic, U_{pl}, energies:

$$U_{tot} = U_{el} + U_{pl} \qquad (1)$$

where U_{el} is obtained from the area enclosed between the unloading segments and displacement axis.[37-39] The elastic recovery and plasticity index were evaluated from the U_{el}/U_{tot} and U_{pl}/U_{tot} ratios, respectively. The mechanical and elastic properties were compared with those of commercial Ti-40Nb alloy. Electrochemical tests were carried out at 37 ºC in a three-electrode cell filled with 100 ml Hank's solution, connected to an Autolab PGSTAT 302N. A Ag/AgCl, KCl (3M) (E = +0.210 V versus NHE) electrode, a platinum spiral and the sample were used as the reference, the counter and the working electrode, respectively. A copper wire was welded to

6

one side of the sample disk, afterwards embedded in a non-conductive resin and finally carefully polished (up to 4000 SiC grit followed by diamond paste of 6, 3 and 1 μm) leaving only a net surface for corrosion tests. The solution was de-aerated with Argon flux after each measurement. The open-circuit potential (E_{OCP}) versus time was recorded for 30 min and immediately afterwards the potential was scanned from (E_{OCP} −0.3) V to + 0.8 V at a scan rate of 0.5 mV/s. All tests have been repeated several times to ensure reliability of the data. The biological behavior of $Ti_{45}Zr_{15}Pd_{35-x}Si_5Nb_x$ (x=0, 5 at. %) alloys were tested in cell culture, analyzing cell viability, morphology and adhesion. Alloy disks were glued individually onto a glass coverslip with silicone (Bayer), introduced into a 4-multiwell culture plate and sterilized under UV light for at least 2 h. Once sterilized, 50,000 cells from the human osteosarcoma cell line Saos-2 (ATCC) were cultured into each well in Dulbecco's modified Eagle medium (Invitrogen) with 10% foetal bovine serum (Gibco) in standard conditions (37°C and 5% CO_2) for 24 h. For all experiments three groups were analyzed: cells grown on top of the alloy disk, cells grown on the coverslip in presence of the alloy and cells grown in absence of the alloy (control culture). All experiments were conducted in triplicate. Cell viability was analysed by Live/Dead Viability/Cytotoxicity Kit for mammalian cells (Invitrogen), according to the manufacturer's protocol. Images from different regions of the alloy disk and its coverslip, and from the control culture were captured using an Olympus IX71 inverted microscope equipped with epifluorescence. A minimum of 200 cells were analyzed per group. Data were analysed for significance using the Fisher's exact test for comparison between groups. Statistical significance was considered when $p < 0.05$. For cell morphology analyses, cultured cells were rinsed twice in phosphate buffered saline (PBS), fixed in 4% paraformaldehyde (Sigma) in PBS for 45 min at room temperature (RT) and rinsed twice in PBS. Cell dehydration was performed in a series of ethanol (50, 70, 90 and twice 100%), 7 min

7

each. Finally, samples were dried using hexamethyl disilazane (HMDS; Electron Microscopy Sciences) for 15 min, mounted on special stubs and analysed using SEM (Zeiss Merlin). Cell adhesion was determined by the presence of focal contacts. Phalloidin was used to visualize actin filaments whereas an antibody against vinculin was used to detect the focal contacts. Cells (50,000) were seeded into a well containing an alloy and, after 24 h of culture cells were fixed in 4% paraformaldehyde in PBS for 45 min at RT, permeabilised with 0.1% Triton X-100 (Sigma) in PBS for 15 min and blocked for 25 min with 1% PBS-bovine serum albumin (Sigma) at RT. Samples were then incubated with a mouse anti-vinculin primary antibody (Chemicon) for 60 min at RT and washed with 1% PBS-BSA. Next, samples were incubated with a mixture of Alexa fluor 594-conjugated phalloidin (Invitrogen), Alexa fluor 488 goat anti-mouse IgG1 (Sigma) and Hoechst 33258 (Sigma) for 60 min at RT. Finally, samples were washed in 1% PBS-BSA and air dried. Samples were mounted on specific bottom glass dishes (MatTek) using Fluoroprep mounting solution (Biomerieux) and imaged in a confocal laser scanning microscope (Leica SP5).

RESULTS AND DISCUSSION

Microstructure

The XRD patterns of the as-cast (a) $Ti_{45}Zr_{15}Pd_{35}Si_5$ and (b) $Ti_{45}Zr_{15}Pd_{30}Si_5Nb_5$ alloys are shown in Figure 1. The most intense XRD diffraction peaks belong to the cubic β-Ti phase (Im3m). The remaining peaks indicate the presence of the following phases: hexagonal α-Ti (P63/mmc), cubic TiPd (Pm3m), cubic PdZr (Fm3m), and hexagonal $(Ti,Zr)_5Si_3$ (P63/mcm) phases. Although the α- and β-Ti reflections are partially overlapped, the relative peak intensities do indicate that the β-Ti phase is predominant (as noticed on comparing the JCPDS 44-1288 and 23-1300 cards and further confirmed by Rietveld fitting). Notice also that most of the TiPd reflections are also

8

overlapped with the β-Ti peaks. Nevertheless, the peak located at $2\theta = 48.87^\circ$ which is univocally assigned to the TiPd phase, indicates that its phase amount is rather low. Although both patterns consist of the same phases, the reflections in the diffractogram of $Ti_{45}Zr_{15}Pd_{30}Si_5Nb_5$ are sharper and more intense, particularly those belonging to the β-Ti phase. This suggests the presence of bigger crystals (and lower microstrains) and possibly larger volume fraction of β-Ti. Taking into account the atomic radii of Ti (1.60 Å), Zr (1.75 Å), Pd (1.39 Å), Si (1.11 Å) and Nb (1.65 Å) and their percentages, the following considerations can be done. The tabulated lattice parameter of the β-Ti phase is considerably larger ($a_{tab.} = 3.30$ Å) than the calculated value ($a_{cal.} = 3.212$ Å), indicating the probable dissolution of Pd in the β-Ti cubic lattice. Moreover, the tabulated cell parameter of TiPd phases ($a_{tab.} = 3.19$ Å) is slightly lower than the calculated one ($a_{cal.} = 3.22$ Å). This difference can be explained by either the presence of substitutional Zr atoms in Ti positions or by slight variations in the stoichiometry (i.e., the concentration of Ti atoms is slightly larger than 1). Figure 2 shows the SEM images (obtained using backscattered electrons) of the Ti-Zr-Pd-Si-(Nb) alloys. These materials exhibit similar composite-like microstructure with the presence of at least five different phases (see Figure 3). The images are representative of the microstructure at the centre of the discs and show four different regions with varying grey scale (A-D), together with eutectic lamellae (E). A zoomed detail of the eutectic matrix is provided as insets of Figure 2(a, b). No significant differences were observed between $Ti_{45}Zr_{15}Pd_{35}Si_5$ and $Ti_{45}Zr_{15}Pd_{30}Si_5Nb_5$ alloys. Energy dispersive x-ray (EDX) mapping analysis was performed on selected zones of the samples to determine the distribution of Ti, Zr, Pd, Si and Nb elements (Figure 3a-d). The EDX mapping of Ti-Zr-Pd-Si-(Nb) alloys (Figure 3(a,c)) indicates that the light grey precipitates (zone A) are rich in palladium, whereas the black precipitates (zone B) are enriched in Zr, Si (and Nb in case of Ti-Zr-Pd-Si-Nb sample) (see Table I). Ti is almost equally

9

distributed everywhere, although a larger amount was found in the dark grey region (zone C) (Table I). On the other hand, the EDX mapping of eutectic regions in Ti-Zr-Pd-Si-(Nb) alloys (Figure 3(b, d)) reveals that the interfaces between the eutectic domains (zone D) are rich in Zr, whilst larger amounts of Si (and Nb in case of Ti-Zr-Pd-Si-Nb sample) are concentrated within the eutectic lamellae (zone E). Unfortunately, for this sample, the EDX spot analyses were not conclusive because of its fine microstructure, so that very similar element percentages were observed in both regions, this is, the interfaces between the eutectic domains and eutectic lamellae. Taking XRD and EDX results of Ti-Zr-Pd-Si-(Nb) system into account, the following considerations can be made. As for the $Ti_{45}Zr_{15}Pd_{35}Si_5$ alloy is concerned, zone A likely corresponds to TiPd phase with Zr in solid solution. This is supported by both the smaller cell parameter of the TiPd phase compared with the tabulated value and the moderate content of Zr determined by EDX (Table I). Besides, zone B could be assigned to $(Ti, Zr)_5Si_3$ phase, whereas the zone C can be mainly linked to α- or β-Ti phases. For the $Ti_{45}Zr_{15}Pd_{30}Si_5Nb_5$ alloy, the zone D could belong to PdZr phase, while the other phases would be forming the surrounding eutectic domains (zone E). In order to gain deeper insight of the microstructure character of the eutectic region, the Ti-Zr-Pd-Si alloy was analysed by TEM (Figure 4 (a)-(d)). Figure 4(a) shows a TEM image of the eutectic lamellae. The corresponding selected area electron diffraction (SAED) pattern indicates that the eutectic colonies are composed of α-Ti, β-Ti and cubic TiPd phases (Fig. 4(b)). Zoomed details of the bright and dark regions suggest that the former is actually composed of α-Ti and β-Ti phases whereas TiPd phase is present in the dark region. The crystal enclosed in the white box of the HRTEM image of Figure 4(c) actually corresponds to α-Ti phase, as corroborated by insets (I) and (II). Namely, the interplanar distance of the spots in the FFT (inset I) match the α-Ti phase and the same holds for the fringes in the Fourier filter

10

Mechanical characterization

Figure 5 shows representative nanoindentation load-displacement (P–h) curves of the $Ti_{45}Zr_{15}Pd_{35}Si_5$, $Ti_{45}Zr_{15}Pd_{30}Si_5Nb_5$ and commercial Ti–40Nb alloys, measured to a maximum load of 250 mN. The Ti-40Nb alloy was used for a comparison aim. Indentations using such a high load are large enough to embrace all the existing phases (A-E), so that the obtained hardness values are representative of the average strength of the alloy. A typical indent made in $Ti_{45}Zr_{15}Pd_{35}Si_5$ is shown as an inset in Figure 5. Table II shows that the addition of Nb decreases the Young's modulus from about 117 GPa to a 85 GPa value, which is just slightly larger than the value of the commercial Ti-40Nb alloy (72 GPa). Ultrasonic measurements were performed to compare the values of Young's modulus with those of nanoindentation tests. Additionally, the other elastic properties values (the Poisson's coefficient (v), Young's modulus (E), shear modulus (G), and bulk modulus (K)) were also evaluated (Table III). The Young's modulus significantly decreases from 100 GPa for $Ti_{45}Zr_{15}Pd_{35}Si_5$ to 87.3 GPa for $Ti_{45}Zr_{15}Pd_{30}Si_5Nb_5$ alloy, in agreement with nanoindentation data. Besides the elastic modulus, the values of hardness were also determined by nanoindentation tests. Remarkably, both the $Ti_{45}Zr_{15}Pd_{35}Si_5$ and $Ti_{45}Zr_{15}Pd_{30}Si_5Nb_5$ alloys are significantly harder than Ti-40Nb (by a factor 5 and 4, respectively). The $Ti_{45}Zr_{15}Pd_{35}Si_5$ alloy is mechanically harder than the $Ti_{45}Zr_{15}Pd_{30}Si_5Nb_5$ and Ti-40Nb alloys, as can be deduced from (P–h) curve from the smallest values of penetration depth using force of 250 mN (Figure 5). It is worth mentioning that the hardness of $Ti_{45}Zr_{15}Pd_{35}Si_5$ and $Ti_{45}Zr_{15}Pd_{30}Si_5Nb_5$ alloys are also larger than that of Ti–39.3Nb–13.3Zr–

11

10.7Ta and Ti–31.0Fe–9.0Sn alloys, which has been previously investigated as suitable material for bone replacement due to its good mechanical properties.[40] Difference in the mechanical response between $Ti_{45}Zr_{15}Pd_{35}Si_5$ and $Ti_{45}Zr_{15}Pd_{30}Si_5Nb_5$ alloys can be explained by the relative fraction of bcc β phase, the chemical composition and the difference in crystal size. In particular, $Ti_{45}Zr_{15}Pd_{30}Si_5Nb_5$ alloy has larger fraction of bcc β phase and larger crystal sizes, resulting in lower hardness than for $Ti_{45}Zr_{15}Pd_{35}Si_5$. In materials with small crystallites, the grain boundaries hinder the dislocation motion and increase the stress concentration and dislocation pile up at the grain boundaries, ultimately leading to increased hardness.[41] Niobium is considered to be the strongest beta stabilizer, effectively decreasing Young's modulus of titanium alloys.[42] In fact, the Young's modulus of commercial Ti-40Nb, composed only of β -Ti, is the lowest among the examined alloys. According to Abdi et al.,[43] addition of Nb to $(Ti,Zr)_5Si_3$ phase causes a local decrease of E_r as compared to the Nb-free alloy. This is to some extend expected since the Young's modulus of Nb is lower than that of Ti.

Listed in Table II are the ratios of H/E_r and H^3/E_r^2 for all investigated alloys. These parameters are associated with wear resistance and are important to estimate the lifetime of the implant. H/E_r indicates the elastic strain to failure[44] while H^3/E_r^2 is related to the resistance of a material to plastic deformation in loaded contact.[45] Due to large hardness and relatively low values of Young's modulus of $Ti_{45}Zr_{15}Pd_{35}Si_5$ and $Ti_{45}Zr_{15}Pd_{30}Si_5Nb_5$, the values of H/E_r and H^3/E_r^2 are almost twice larger than those of Ti-40Nb. In fact, the elastic recovery, U_{el}/U_{tot}, is also higher in the new Ti-Zr-Pd-Si-(Nb) system. Hence, these materials would be more resistant to impact loading than Ti–40Nb.[46] With the aim to study the contribution of the individual phases or regions, to the overall mechanical response, nanoindentation tests applying a maximum load of 3 mN were carried out for $Ti_{45}Zr_{15}Pd_{35}Si_5$ sample. The mean values of hardness (H) and reduced

Young's modulus (E_r) corresponding to the different regions (A-D) are listed in Table IV. SEM images of representative indents on each region are presented in Figure 6 (a)-(d). The size of indents is different, being that on the zone B (Figure 6b), the smallest. The values of hardness for the light grey precipitates (Figure 6a), black precipitates (Figure 6b) grey area between the eutectic domains (Figure 6c) and eutectic lamellae (Figure 6d), are equal to 8.9 GPa, 13.7 GPa, 10.1 GPa and 9.7 GPa, respectively (Table IV). The black precipitates are mechanically harder presumably due to the presence of the intermetallic $(Ti,Zr)_5Si_3$ phase. In fact, the hardness of $(Ti, Zr)_5Si_3$ phase has been reported to be 13.7 GPa in Abdi's study.[43] Besides, comparable hardness values were reported by Mitra.[47] Nevertheless, depending on the crystal size the values can slightly vary. For instance, hardness of 12.7 GPa stands for crystal size between 5 to 10 μm, while for smaller crystals (1-2 μm), the hardness values increase up to 17.2 GPa.[47] On the contrary, the hardness of the light grey precipitates (TiPd phase) and eutectic lamellae (phase mixture), are the lowest among all phases (Table IV). Additional consideration can be made on the Young's modulus of white precipitates (TiPd phase) and eutectic lamellae. According to the literature, the calculated Young's modulus of Ti-Pd phase is 80 GPa.[48,49] However, this value increases when it comes to the light grey precipitates region (104 GPa), composed of TiPd phase. This can be explained by the co-existence of α-Ti, which has larger Young's modulus (120 GPa) within this region. Zone C (Figure 6c) which is composed mainly of α-Ti phase exhibits a Young's modulus of 120 GPa. On the contrary, the value of the eutectic is found to be experimentally equal to 110 GPa, which can be attributed to the large amounts of inter-phase boundaries existing in the eutectic regions, as a consequence of phase mixture (Figure 6d).

Corrosion resistance and biocompatibility

13

Prior to the biocompatibility studies, the corrosion resistance of the $Ti_{45}Zr_{15}Pd_{30}Si_5Nb_5$ bulk metallic glass composite was electrochemically evaluated by potentiodynamic polarization in Hank's solution at 37 ºC and the response compared to that of Ti-40Nb sample (taken as a reference). Although $Ti_{45}Zr_{15}Pd_{30}Si_5Nb_5$ is made of several phases and one would a priori expect low corrosion resistance because of the eventual occurrence of galvanic pairs, Figure 7 shows that this is not actually the case. Both samples exhibit similar corrosion current density values and the corrosion potential of $Ti_{45}Zr_{15}Pd_{30}Si_5Nb_5$ sample is shifted toward more positive values compared to Ti-40Nb alloy. Moreover, the current density on the anodic branch is lower for the nanostructured $Ti_{45}Zr_{15}Pd_{30}Si_5Nb_5$ sample.

In order to assess the biocompatibility of the TiZrPdSi(Nb) specimens, cultured human Saos-2 cells were distributed randomly onto the metal alloys and coverslips. The percentage of live cells was higher than 94 % in all groups, and no significant differences were observed between the two alloy compositions, or between them and the coverslip and control plate (Figure 8). These results indicate that the addition of Nb to the alloy composition does not cause any cytotoxic effect, in agreement with the observations done by other authors.[50,51] After 24 h of culture, the cells were attached to the surface of $Ti_{45}Zr_{15}Pd_{35}Si_5$ and $Ti_{45}Zr_{15}Pd_{30}Si_5Nb_5$ alloys and of coverslips, and showed a similar morphology under SEM. Cell density was similar in all cultures analysed and in all cases the cells showed a flattened polygonal morphology with nuclei presenting several nucleoli (Figure 9), an indication of high cellular activity. The actin cytoskeleton structure and its involvement in focal contacts are key to maintain cell adhesion, but also for cell proliferation and differentiation. In this sense, the formation of focal contacts on the surface of the alloy gives information about its biocompatibility. Focal contact analysis showed that Saos-2 cells were completely adhered to the surface of the two alloyed compositions (Figure 10) and coverslips.

14

Actin stress fibres were well-defined in all cases, and some of them extended across the cell and ended in focal contacts. The results indicate that $Ti_{45}Zr_{15}Pd_{35}Si_5$ and $Ti_{45}Zr_{15}Pd_{30}Si_5Nb_5$ alloys allow cell adhesion, in agreement with other studies of biocompatible bulk metallic glasses.[52,53] Furthermore, the formation of focal contacts on the two alloys suggests that ECM proteins, necessary for cell adhesion, can be adsorbed on the alloy surface.[54]

CONCLUSIONS

The microstructure and mechanical properties of nanostructured $Ti_{45}Zr_{15}Pd_{35-x}Si_5Nb_x$ with x = 0, 5 (at. %) alloys have been investigated and compared to those of commercial Ti-40Nb. Both Ti-Zr-Pd-Si-(Nb) rods show a composite-like microstructure consisting of several phases: a predominant β-Ti and additional phases (TiPd, PdZr, α-Ti and $(Ti, Zr)_5Si_3$ intermetallics) in smaller volume fraction, as identified by XRD, SEM and TEM analyses. In terms of mechanical behaviour, nanoindentation experiments reveal that the $Ti_{45}Zr_{15}Pd_{30}Si_5Nb_5$ alloy exhibits lower Young's modulus and hardness than $Ti_{45}Zr_{15}Pd_{35}Si_5$ ($E_{rTi-Zr-Pd-Si} \approx 117$ GPa and $E_{rTi-Zr-Pd-Si-Nb} \approx 85$ GPa). This can be explained by the relative amount of β phase in both alloys and the differences in the mean crystal size values. Remarkably, both alloys exhibit larger values of hardness, wear resistance (indirectly estimated through the H/E_r ratio) and elastic recovery than commercial Ti-40Nb, ($H_{Ti-Zr-Pd-Si} \approx 14.2$ GPa, $H_{Ti-Zr-Pd-Si-Nb} \approx 10.4$ GPa and $H_{Ti-40Nb} \approx 2.7$ GPa. Hence, the newly developed $Ti_{45}Zr_{15}Pd_{35-x}Si_5Nb_x$ alloys with x = 0, 5 (at. %) are interesting for biomedical applications because they combine relatively low Young's modulus (particularly in $Ti_{45}Zr_{15}Pd_{30}Si_5Nb_5$) with large values of hardness. Moreover, $Ti_{45}Zr_{15}Pd_{30}Si_5Nb_5$ sample does not exhibit worse corrosion resistance than commercially used Ti-40Nb alloy in spite of the presence of multiple phases. Additionally, the biological compliance with body system (cell culture, cell viability and cell adhesion) of these two alloys was analysed. Preliminary results of cell viability

performed on several Ti-Zr-Pd-Si-(Nb) discs indicate that the number of live cells is superior to 94 % in both cases. From these outstanding mechanical properties and the excellent biocompatibility these alloys turn out to have a large potential to be used as permanent implants for bone replacement.

REFERENCES

1. Viteri VS, Fuentes E. Titanium and Titanium Alloys as Biomaterials. In: Jürgen Gegner, editor. Tribology – Fundamentals and Advancements, INTECH, InTech: Rijeka, Croatia, Chapter 5. 2013, p.155-181.

2. Liu X, Chu P, Ding C. Surface modification of titanium, titanium alloys, and related materials for biomedical applications. Mater Sci Eng R Reports 2004;47:49–121.

3. Geetha M, Singh AK, Asokamani R, Gogia AK. Ti based biomaterials, the ultimate choice for orthopaedic implants – A review. Prog Mater Sci 2009;54:397–425.

4. Mudali UK, Sridhar TM, Raj B. Corrosion of bio implants. Sadhana 2003;28:601–637.

5. Niinomi M. Mechanical biocompatibilities of titanium alloys for biomedical applications. J Mech Behav Biomed Mater 2008;1:30–42.

6. Long M, Rack HJ. Titanium alloys in total joint replacement – a materials science perspective. Materials 1998;19:1621–1639.

16

7. Wang Y, Chen M, Zhou F, Ma E. High tensile ductility in a nanostructured metal. Nature 2002;419:912–915.

8. Sivakumar M, Kamechi Mudali U, Rajeswali S. In vitro electrochamical investigations of stainless steel for orthopeadic implants applications. J Mater Eng Perform 1994;3:744–759.

9. Lautenschlager EP, Monaghan P. Titanium and titanium alloys as dental materials. Int Dent J 1993;43:245–253.

10. Niinomi M, Nakai M, Hieda J. Development of new metallic alloys for biomedical applications. Acta Biomater 2012;8:3888–3903.

11. Raju A. Effect of equal channel angular extrusion on the shape memory property of Ti-Nb Alloys – doctoral thesis. Korea Advanced Institute of Science and Technology; South Korea, 2010.

12. Wills M, Savory J. Aluminium poisoning: dialysis, encephalopathy, osteomalacia, and anaemia. Lancet 1983;2:29–34.

13. Karimi S. Corrosion behavior of metallic bio-implant alloys. Ph.D Thesis, University of British Columbia, Vancouver, Canada, 2014.

14. Calin M, Gebert A, Ghinea AC, Gostin PF, Abdi S, Mickel C, Eckert J. Designing biocompatible Ti-based metallic glasses for implant applications. Mater Sci Eng C 2013;33:875–883.

15. Ozaki T, Matsumoto H, Watanabe S, Hanada S. Beta Ti alloys with low Young´s modulus. Mater Trans 2004;45:2776–2779.

16. Hao YL, Niinomi M, Kuroda D, Fukunaga K, Zhou YL, Yang R, Suzuki A. Young's modulus and mechanical properties of Ti-29Nb-13Ta-4.6Zr in relation to α'' martensite. Metall Mater Trans A 2002;33:3137–3144.

17. Kuroda D, Niinomi M, Morinaga M, Kato Y, Yashiro T. Design and mechanical properties of new β type titanium alloys for implant materials. Mater Sci Eng A 1998;243:244–249.

18. Hanada S, Matsumoto H, Watanabe S. Mechanical compatibility of titanium implants in hard tissues. Int Congr Ser 2005;1284:239–247.

19. Ma C, Soejima H, Ishihara S, Amiya K, Nishiyama N, Inoue A. New Ti-Based Bulk Glassy Alloys with High Glass-Forming Ability and Superior Mechanical Properties. Mater Trans 2004;45:3223–7.

20. Wang WH, Dong C, Shek CH. Bulk metallic glasses. Mater Sci Eng R Reports. 2004;44:45–89.

17

21. Xie G, Qin F, S Zhu S, Inoue A. Ni-free Ti-based bulk metallic glass with potential for biomedical applications produced by spark plasma sintering. Intermetallic 2012;29:99–104.

22. Wang YB, Li HF, Cheng Y, Zheng YF, Ruan LQ. In vitro and in vivo studies on Ti-based bulk metallic glass as potential dental implant material. Mat Sci Eng C 2013;33:3489–3497.

23. Fornell J, Steenberge N, Vare A, Rossinyol E, Pellicer E, Suriñach S, Baró MD, Sort J. Enhanced mechanical properties and in vitro corrosion behavior of amorphous and devitrified $Ti_{40}Zr_{10}Cu_{38}Pd_{12}$ metallic glass. J Mech Behav Biomed Mat 2011;2:1709–1717.

24. Zheng N. Ni-free Ti-based Bulk Metallic Glasses: Glass Forming Ability and Mechanical Behavior. PhD Thesis: Technischen Universität Dresden, Dresden, Germany, 2014.

25. He G, Eckert J, Löser W, Schultz L. Novel Ti-base nanostructure-dendrite composite with enhanced plasticity. Nat Mater 2003;2:33–37.

26. Weertman JR, Farkas D, Hemker K, Kung H, Mayo M, Mitra R VSH. Structure and Mechanical Behavior of Bulk Nanocrystalline Materials. Mech Behav Nanostructured Mater. 1999;24:44–53.

27. Wu F-F, Chan K C, Jiang S-S, Chen S-H, Wang G. Bulk metallic glass composite with good tensile ductility, high strength and large elastic strain limit. Sci Rep 2014;4:5302

28. Meyers MA, Mishra A, Benson DJ. Mechanical properties of nanocrystalline materials. Prog Mater Sci 2006;51:427–556.

29. Oak J-J, Inoue A. Formation, mechanical properties and corrosion resistance of Ti–Pd base glassy alloys. J Non Cryst Solids 2008;354:1828–1832.

30. Li Y, Yang C, Zhao H, Qu S, Li X, Li Y. New developments of Ti-based alloys for biomedical applications. Materials 2014;7:1709–1800.

31. Afonso CRM, Aleixo GT, Ramirez AJ, Caram R. Influence of cooling rate on microstructure of Ti–Nb alloy for orthopedic implants. Mat Sci Eng C 2007;27:908–913.

32. Niinomi M. Recent research and development in titanium alloys for biomedical applications and healthcare goods. Sci Technol Adv Mater 2003;4:445–454.

33. Gabriel SB, Panaino JVP, Santos ID, Araujo LS, Mei PR, de Almeida LH, Nunes CA. Characterization of a new beta titanium alloy, Ti–12Mo–3Nb, for biomedical applications. J Alloys Compd 2012;5365:S208–S210.

18

34. Song Y, Xu DS, Yang R, Li D, Wu WT, Guo ZX. Theoretical study of the effects of alloying elements on the strength and modulus of β-type bio-titanium alloys. Mater Sci Eng A 1999;260:269–274.

35. Fischer-Cripps AC. Nanoindentation; Mechanical Engineering Series. Third. New York: Springer; 2011.

36. Oliver WC, Pharr GM. An improved technique for determing hardness and elastic modulus. J Mater Res 1992;7:1564–1583.

37. Pellicer E, Varea A, Pané S, Nelson BJ, Menéndez E, Estrader M, Suriñach S, Baró MD, Nogués J, Sort J. Nanocrystalline electroplated Cu–Ni: metallic thin films with enhanced mechanical properties and tunable magnetic behavior. Adv Funct Mater 2010;20:983–991.

38. Bao YW, Wang W, Zhou YC. Investigation of the relationship between elastic modulus and hardness based on depth-sensing indentation measurements. Acta Mater 2004;52:5397–5404.

39. Fornell J, Surinach S, Baró MD, Sort J. Identation plastic work and large compression plasticity in situ nanocrystallized $Zr_{62}Cu_{18}Ni_{10}Al_{10}$ bulk metallic glass. J Alloys Compd. 2011;509S:S87–S91.

40. Hynowska A, Pellicer E, Fornell J, González S, van Steenberge N, Suriñach S, Gebert A, Calin M, Eckert J, Baró MD, Sort J. Nanostructured β − phase Ti–31.0Fe–9.0Sn and sub − μm structured Ti–39.3Nb–13.3Zr–10.7Ta alloys for biomedical applications: Microstructure benefits on the mechanical and corrosion performances. Mater Sci Eng C 2012;32:2418–2425.

41. Hall EO. The deformation and ageing of mild steel III, Discussion of results. Proc Phys Soc. 1951;64:747–753.

42. Brailovski V, Prokoshkin S, Gauthier M, Inaekyan K, Dubinskiy S, Petrzhik M, Filonov M. Bulk and porous metastable beta Ti–Nb–Zr-(Ta) alloys for biomedical applications. Mater Sci Eng C 2011;31:643–657.

43. Abdi S, Khoshkhoo MS, Shuleshova O, Bönisch M, Calin M, Schultz L, Eckert J, Baró MD, Sort J, Gebert A. Effect of Nb addition on microstructure evolution and nanomechanical properties of a glass-forming Ti–Zr–Si alloy. Intermetallics 2014;46:156–163.

44. Leyland A, Matthews A. On the significance of the H/E ratio in wear control: a nanocomposite coating approach to optimised tribological behaviour. Wear 2000;246:1–11.

19

45. Musil J, Kunc F, Zeman H, Poláková H. Relationships between hardness, young's modulus and elastic recovery in hard nanocomposite coatings. Surf Coat Technol 2002;154:304–313.

46. Milman YV. Plasticity characteristic obtained by indentation. J Phys D Appl Phys 2008;41:074013.

47. Mitra R. Microstructure and mechanical behavior of reaction hot – pressed titanium silicide and titanium silicide – based alloys and composites. Metall Mater Trans A 1998;29:1629–1641.

48. Bihlmayer G, Eibler R, Neckel A. Martensitic phase transformation and electronic structure of NiTi and PdTi. Philos Mag Part B 1996;73:511–524.

49. Chen X-Q, Fu CL, Morris JR. The electronic, elastic, and structural properties of Ti–Pd intermetallics and associated hydrides from first principles calculations. Intermetallics 2010;18:998–1006.

50. Miura K, Yamada N, Hanada S, Jung T-K, Itoi E. The bone tissue compatibility of a new Ti-Nb-Sn alloy with a low Young's modulus. Acta Biomater 2011;7:2320–2326.

51. Da Silva LM, Claro APRA, Donato TAG, Arana-Chavez VE, Moraes JCS, Buzalaf MAR, Grandini CR. Influence of heat treatment and oxygen doping on the mechanical properties and biocompatibility of titanium-niobium binary alloys. Artif Organs 2011;35:516–521.

52. Blanquer A, Pellicer E, Hynowska A, Barrios L, Ibáñez E, Baró MD, Sort J, Nogués C. In vitro biocompatibility assessment of $Ti_{40}Cu_{38}Zr_{10}Pd_{12}$ bulk metallic glass. J Mater Sci Mater Med 2013;25:163–172.

53. Huang L, Cao Z, Meyer HM, Liaw PK, Garlea E, Dunlap JR, Zhang T, He W. Responses of bone-forming cells on pre-immersed Zr-based bulk metallic glasses: Effects of composition and roughness. Acta Biomater 2011;7:395–405.

54. Bacakova L. Modulation of cell adhesion, proliferation and differentiation on materials designed for body implants. Biotechnol Adv 2011;29:739–767.

Figures and Tables Captions

FIGURE 1. X-ray diffraction patterns (XRD) corresponding to the as-cast (a) $Ti_{45}Zr_{15}Pd_{35}Si_5$ and (b) $Ti_{45}Zr_{15}Pd_{30}Si_5Nb_5$ alloys.

20

FIGURE 2. Scanning electron microscope (SEM) images (backscattered electrons) of the as-cast (a) $Ti_{45}Zr_{15}Pd_{35}Si_5$ and (b) $Ti_{45}Zr_{15}Pd_{30}Si_5Nb_5$ alloys taken at the centre of the discs. Shown as insets (a, b), are zoomed details of the eutectic region.

FIGURE 3. SEM (backscattered electrons) images and corresponding energy dispersive x-ray mapping of Ti, Zr, Pd, Si (and Nb) elements in $Ti_{45}Zr_{15}Pd_{35}Si_5$ and $Ti_{45}Zr_{15}Pd_{30}Si_5Nb_5$ discs taken at central part of the rod showing (a, c) A, B and C regions and (b, d) D, E regions.

FIGURE 4. (a) Transmission electron micrograph (TEM) of the eutectic matrix in the $Ti_{45}Zr_{15}Pd_{35}Si_5$ alloy, (b) selected area electron diffraction pattern of image (a), revealing the existence of β-Ti, α-Ti and TiPd phases. (c) Zoomed detail of the bright region of the eutectic matrix; insets (I) and (II) are the FFT and Fourier filter reconstruction, respectively, of the crystal enclosed in the white box, which belongs to α-Ti. (d) Zoomed detail of the dark region of the eutectic matrix; inset (I) is the FFT of the crystal enclosed in the white box, which belongs to TiPd. The white arrows depicted in insets (I) point to the diffraction spots, with interplanar distances matching α-Ti (d = 0.2276 nm) and TiPd (d = 0.3138 nm for upper left arrow).

FIGURE 5. Load-displacement (P-h) nanoindentation curves for Ti-40Nb, $Ti_{45}Zr_{15}Pd_{35}Si_5$ and $Ti_{45}Zr_{15}Pd_{30}Si_5Nb_5$ alloys obtained applying a maximum force, ($P_{max.}$ = 250 mN). Shown in the inset is a backscattered SEM image of an indent performed on the $Ti_{45}Zr_{15}Pd_{35}Si_5$ alloy. It can be seen that the indent embraces all existing phases (A-E).

FIGURE 6. Representative SEM (backscattered electrons) images belonging to $Ti_{45}Zr_{15}Pd_{35}Si_5$ composition. Shown in the pictures [(a)-(d)] are the indents inside: (a) the light grey precipitates, (b) black precipitates, (c) grey area between the eutectic domain and (d) the eutectic lamellae, (P_{Max} = 3 mN). The size of the imprints on the D regions was larger than the actual size of the region and therefore the corresponding SEM image is not presented.

FIGURE 7. Potentiodynamic polarization curves of the $Ti_{45}Zr_{15}Pd_{30}Si_5Nb_5$ and Ti-40Nb alloys immersed in Hank's solution at 37 ºC.

FIGURE 8. Mean percentage of live cells attached to the surface of the tested alloys, their coverslips and in control cultures.

FIGURE 9. SEM images of Saos-2 cells on the surface of alloy disks; (a) $Ti_{45}Zr_{15}Pd_{35}Si_5$ and (b) $Ti_{45}Zr_{15}Pd_{30}Si_5Nb_5$. Flattened cells with polygonal morphologies showing nuclei with several nucleoli can be observed in all cases.

FIGURE 10. Cells adhered on the surface of the alloys. (a) $Ti_{45}Zr_{15}Pd_{35}Si_5$ and (b) $Ti_{45}Zr_{15}Pd_{30}Si_5Nb_5$. Stress fibres (actin; red), focal contacts (vinculin; green) and nuclei (DNA; blue) can be observed.

TABLE I. Energy dispersive X-ray (EDX) compositional analyses corresponding to the selected areas shown for as-cast $Ti_{45}Zr_{15}Pd_{35}Si_5$ alloy (Figure 3a, c) and $Ti_{45}Zr_{15}Pd_{30}Si_5Nb_5$ (Figure 3b, d). Data estimated with the error of 1-2 %.

TABLE II. Summary of the mechanical properties (H, E_r, H/E_r, H^3/E^2_r, U_{el}/U_{tot}, and U_{pl}/U_{tot} denote hardness, reduced Young's modulus, elastic, plastic and total indentation energies, respectively), assessed by nanoindentation measurements, corresponding to the $Ti_{45}Zr_{15}Pd_{35}Si_5$, $Ti_{45}Zr_{15}Pd_{30}Si_5Nb_5$ alloys and Ti–40Nb ($F_{max.} = 250$ mN).

TABLE III. Summary of the elastic properties (v, E_{Acoust}, G and K denote the Poisson's coefficient, Young's modulus, shear modulus and bulk modulus, respectively) of the as-cast $Ti_{45}Zr_{15}Pd_{35-x}Si_5Nb_x$ ($x = 0, 5$) alloys. Results for the commercial Ti–40Nb are shown for comparison purposes.

TABLE IV. The mean values of hardness (H) and reduced Young's modulus (E_r) calculated for the indents in different regions in $Ti_{45}Zr_{15}Pd_{35}Si_5$ [see examples in Fig. 6 (a)-(d)]. The mean values of H and E_r are the result of 10 nanoindentation tests in each region.
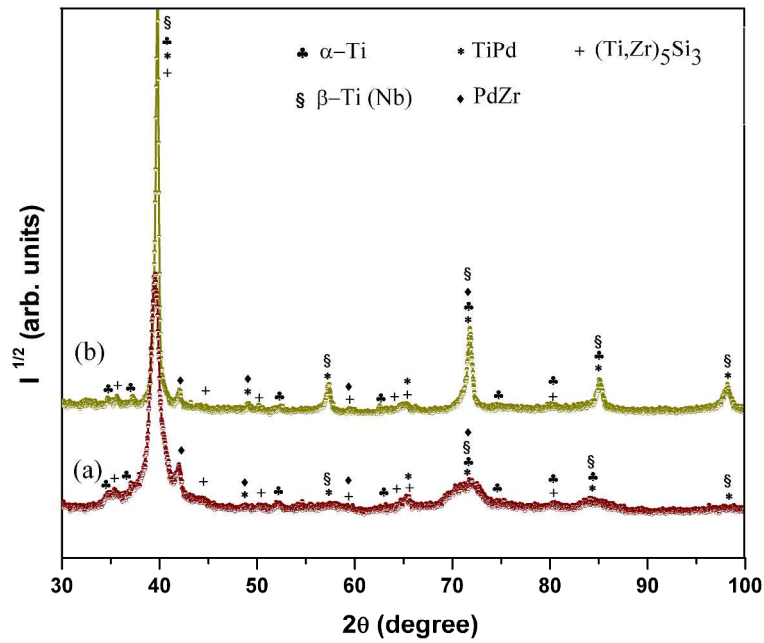
22

Figure 1. X-ray diffraction patterns (XRD) corresponding to the as-cast (a) $Ti_{45}Zr_{15}Pd_{35}Si_5$ and (b) $Ti_{45}Zr_{15}Pd_{30}Si_5Nb_5$ alloys.
1083x829mm (150 x 150 DPI)
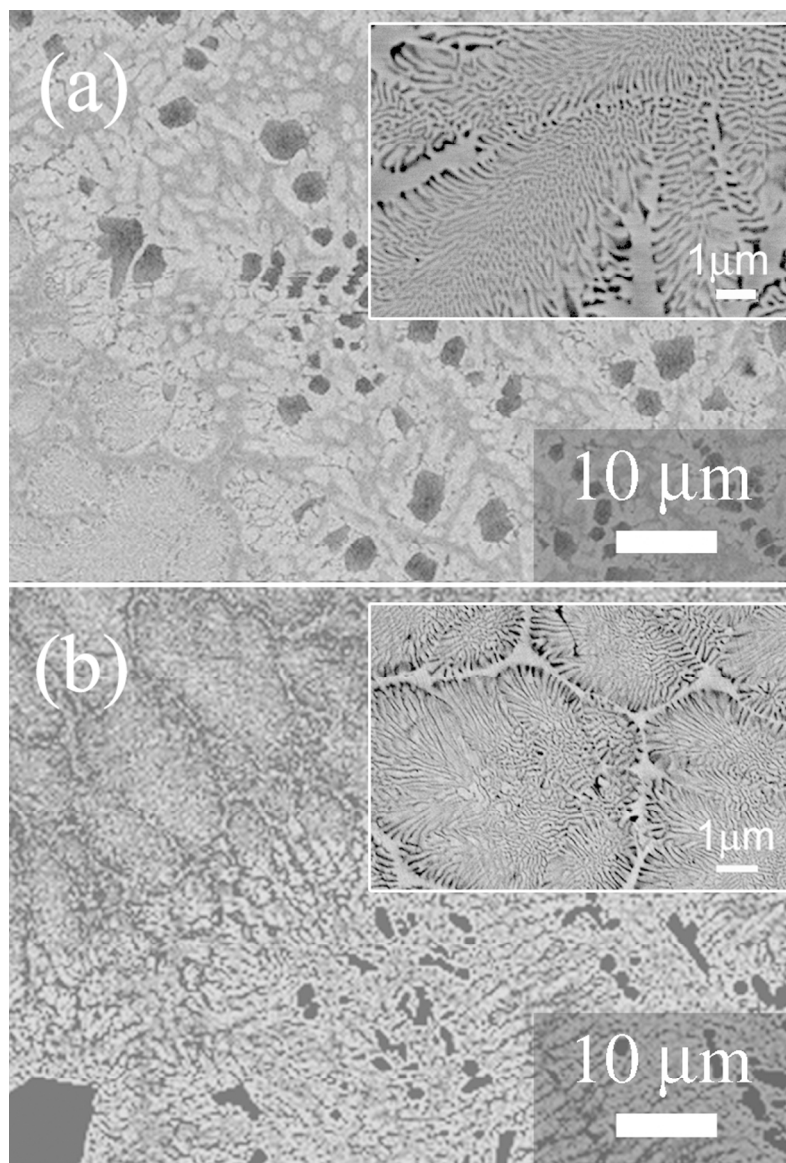
Figure 2. Scanning electron microscope (SEM) images (backscattered electrons) of the as-cast (a)
$Ti_{45}Zr_{15}Pd_{35}Si_5$ and (b) $Ti_{45}Zr_{15}Pd_{30}Si_5Nb_5$
alloys taken at the centre of the discs. Shown as insets (a, b), are
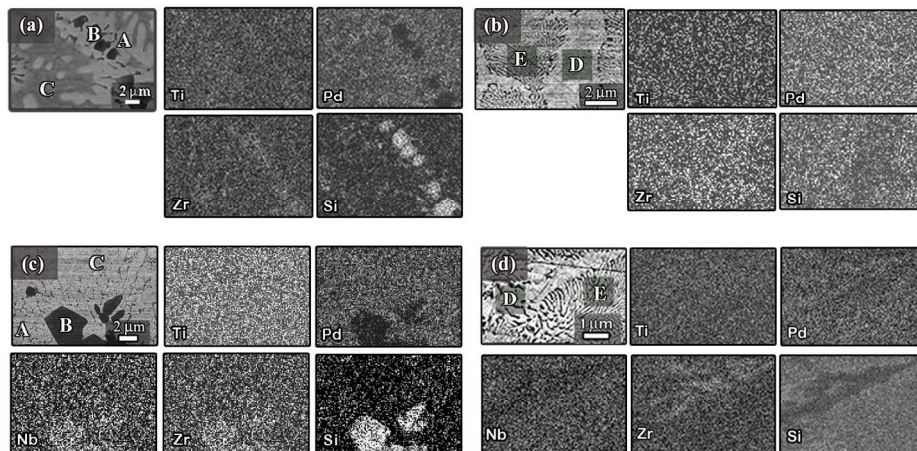zoomed details of the eutectic region.
71x107mm (300 x 300 DPI)

Figure 3. SEM (backscattered electrons) images and corresponding energy dispersive x-ray mapping of Ti, Zr, Pd, Si (and Nb) elements in $Ti_{45}Zr_{15}Pd_{35}Si_5$ and $Ti_{45}Zr_{15}Pd_{30}Si_5Nb_5$ discs taken at central part of the rod showing (a, c) A, B and C regions and (b, d) D, E regions.
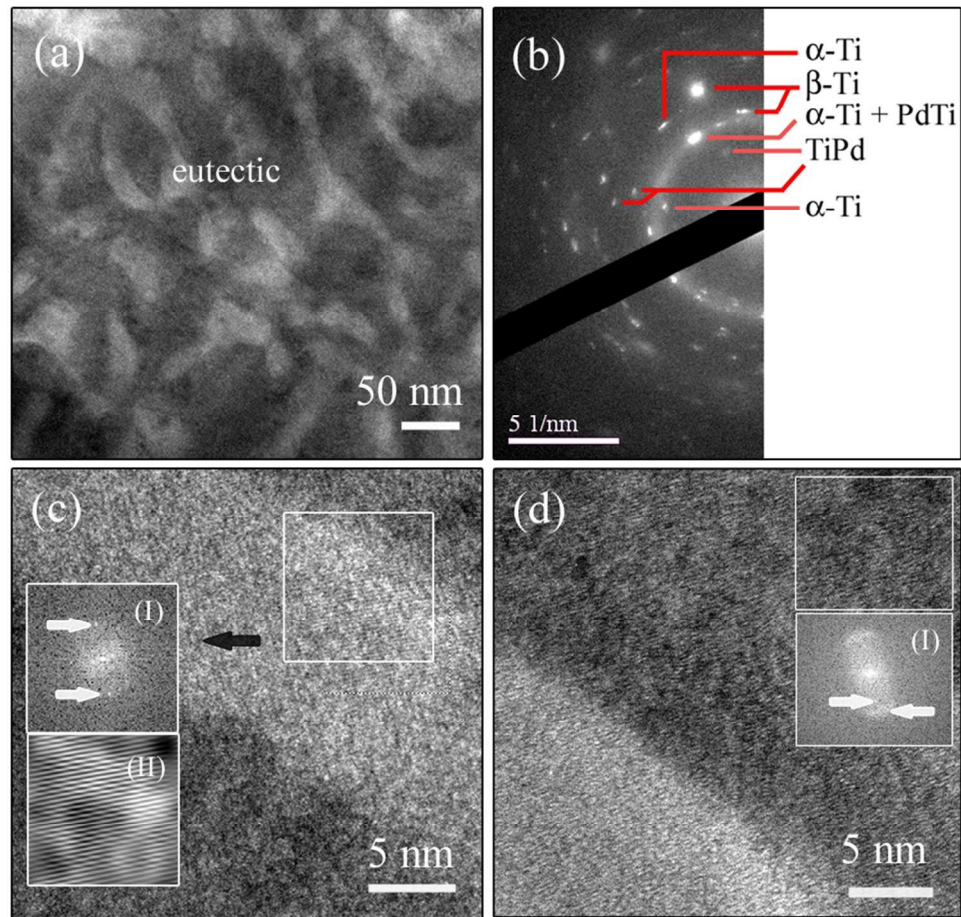140x70mm (300 x 300 DPI)

Figure 4. (a) Transmission electron micrograph (TEM) of the eutectic matrix in the $Ti_{45}Zr_{15}Pd_{35}Si_5$ alloy, (b) selected area electron diffraction pattern of image (a), revealing the existence of α-Ti, β-Ti and TiPd phases. (c) Zoomed detail of the bright region of the eutectic matrix; insets (I) and (II) are the FFT and Fourier filter reconstruction, respectively, of the crystal enclosed in the white box, which belongs to α-Ti. (d) Zoomed detail of the dark region of the eutectic matrix; inset (I) is the FFT of the crystal enclosed in the white box, which belongs to TiPd. The white arrows depicted in insets (I) point to the diffraction spots, with interplanar distances matching α-Ti (d = 0.2276 nm) and TiPd (d = 0.3138 nm for upper left arrow).
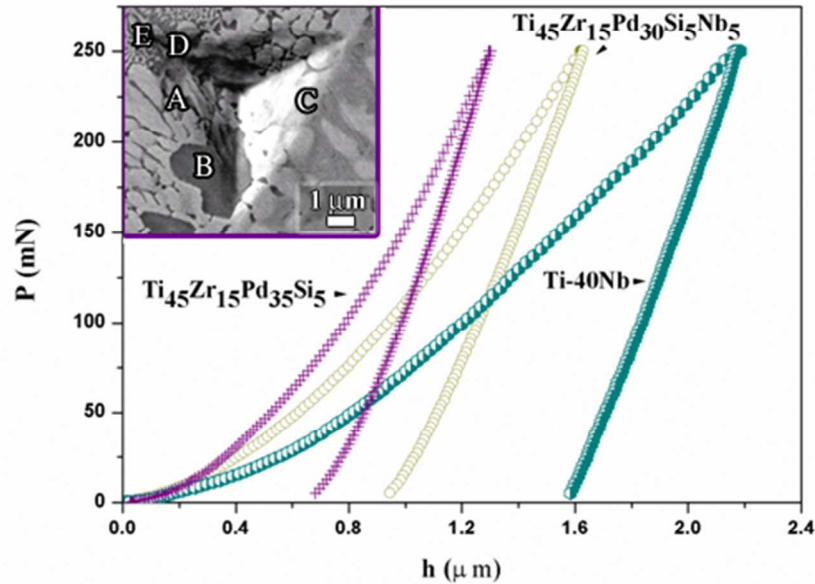84x77mm (300 x 300 DPI)

Figure 5. Load-displacement (P-h) nanoindentation curves for Ti-40Nb, Ti$_{45}$Zr$_{15}$Pd$_{35}$Si$_5$ and Ti$_{45}$Zr$_{15}$Pd$_{30}$Si$_5$Nb$_5$ alloys obtained applying a maximum force, (P$_{max.}$ = 250 mN). Shown in the inset is a backscattered SEM image of an indent performed on the Ti$_{45}$Zr$_{15}$Pd$_{35}$Si$_5$ alloy. It can be seen that the indent embraces all existing phases (A-E).
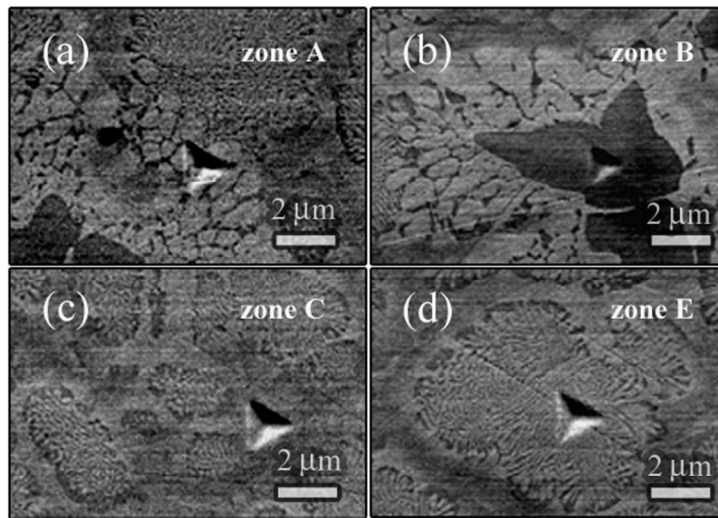212x148mm (72 x 72 DPI)

Figure 6. Representative SEM (backscattered electrons) images belonging to $Ti_{45}Zr_{15}Pd_{35}Si_5$ composition. Shown in the pictures [(a)-(d)] are the indents inside: (a) the light grey precipitates, (b) black precipitates, (c) grey area between the eutectic domain and (d) the eutectic lamellae, ($P_{Max.}$ = 3 mN). The size of the imprints on the D regions was larger than the actual size of the region and therefore the corresponding SEM image is not presented.
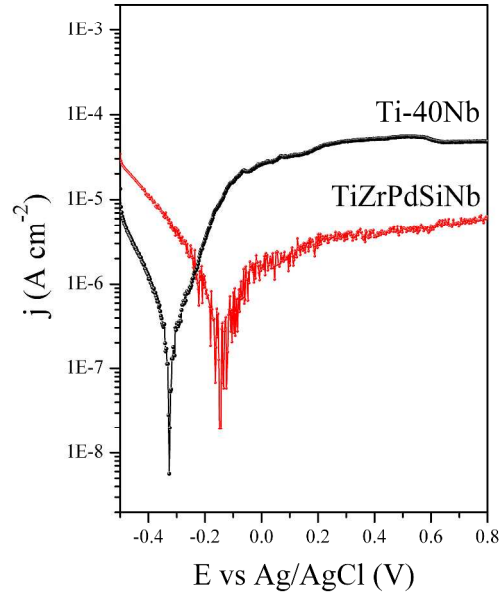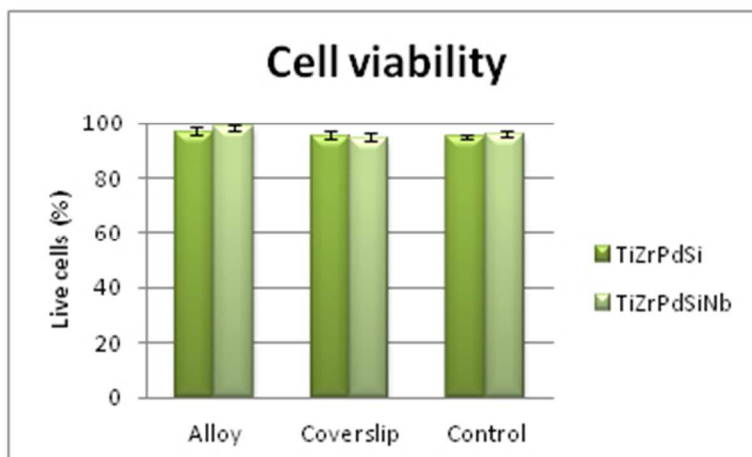146x100mm (150 x 150 DPI)

Figure 7. Potentiodynamic polarization curves of the $Ti_{45}Zr_{15}Pd_{30}Si_5Nb_5$ and Ti-40Nb alloys immersed in Hank's solution at 37 ºC.
1188x840mm (150 x 150 DPI)

Figure 8. Mean percentage of live cells attached to the surface of the tested alloys, their coverslips and in control cultures.
134x81mm (72 x 72 DPI)
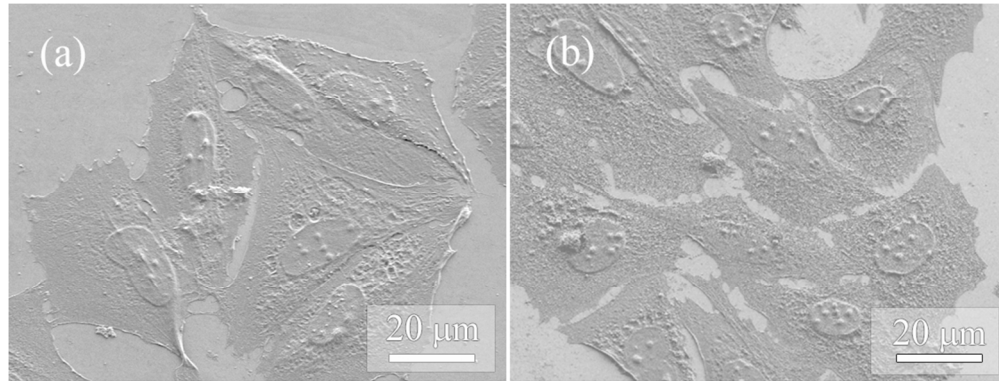
Figure 9. SEM images of Saos-2 cells on the surface of alloy disks; (a) $Ti_{45}Zr_{15}Pd_{35}Si_5$ and (b) $Ti_{45}Zr_{15}Pd_{30}Si_5Nb_5$. Flattened cells with polygonal morphologies showing nuclei with several nucleoli can be observed in all cases.
398x151mm (72 x 72 DPI)

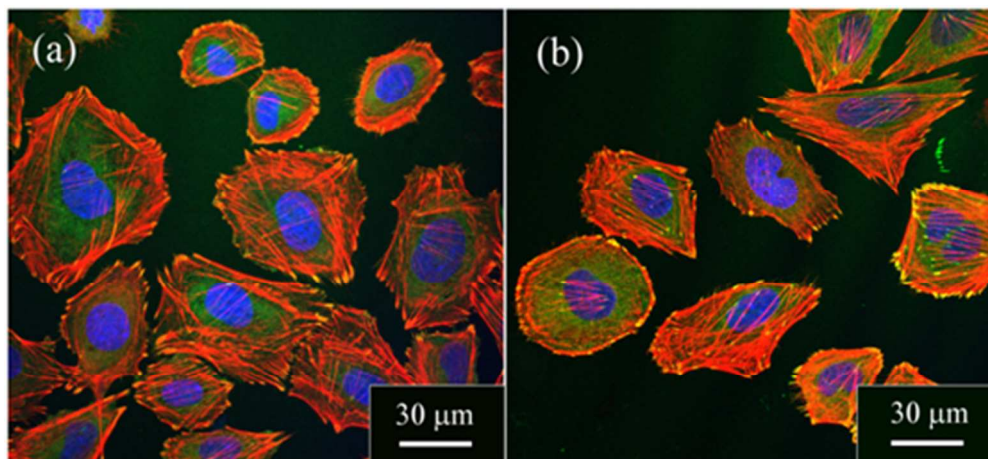Figure 10. Cells adhered on the surface of the alloys. (a) $Ti_{45}Zr_{15}Pd_{35}Si_5$ and (b) $Ti_{45}Zr_{15}Pd_{30}Si_5Nb_5$. Stress fibres (actin; red), focal contacts (vinculin; green) and nuclei (DNA; blue) can be observed.
190x88mm (72 x 72 DPI)

TABLE I.

	Element concentration (at. %)								
	Ti-Zr-Pd-Si				Ti-Zr-Pd-Si-Nb				
	Ti	**Pd**	**Zr**	**Si**	**Ti**	**Pd**	**Zr**	**Si**	**Nb**
Nominal comp.	45	35	15	5	45	30	15	5	5
Zone(s)	Fig. 3 (a)				Fig. 3 (c)				
A	40	45	15	< 1	38	40	16	1	5
B	41	9	21	29	33	6	20	31	10
C	49	35	14	1	44	35	16	<1	4
Zone(s)	Fig. 3 (b)				Fig. 3 (d)				
D	43	32	24	<1	43	33	21	1	2
E	43	36	16	5	40	33	17	5	5

TABLE II.

Sample	H (GPa)	E_r (GPa)	H/E_r	H^3/E_r^2 (GPa)	U_{el}/U_{tot}	U_{pl}/U_{tot}
$Ti_{45}Zr_{15}Pd_{35}Si_5$	14.2 ± 0.5	117 ± 5	0.122 ± 0.005	0.211 ± 0.030	0.586 ± 0.029	0.414 ± 0.021
$Ti_{45}Zr_{15}Pd_{30}Si_5Nb_5$	10.4 ± 0.3	85 ± 2	0.123 ± 0.003	0.156 ± 0.016	0.543 ± 0.017	0.475 ± 0.015
Ti-40Nb	2.7 ± 0.1	72 ± 1	0.038 ± 0.001	0.004 ± 0.001	0.225 ± 0.004	0.775 ± 0.013

For Peer Review

TABLE III.

Sample	ν	$E_{Acoust.}$ (GPa)	G (GPa)	K (GPa)
$Ti_{45}Zr_{15}Pd_{35}Si_5$	0.405 ± 0.003	100.0 ± 0.1	30.1 ± 0.1	148.6 ± 0.7
$Ti_{45}Zr_{15}Pd_{30}Si_5Nb_5$	0.397 ± 0.001	87.3 ± 0.2	31.3 ± 0.1	139.5 ± 0.2
Ti-40Nb	0.403 ± 0.001	73.8 ± 0.1	26.3 ± 0.1	126.6 ± 0.1

TABLE IV.

Specified area of nanoindents	H (GPa)	E_r (GPa)
Fig 6 (**a**) – light grey precipitates (zone A)	8.9 ± 0.3	104.3 ± 2.1
Fig 6 (**b**) – black precipitates (zone B)	13.7 ± 1.5	135.5 ± 2.6
Fig 6 (**c**) – grey area between the eutectic domains (zone C)	10.1 ± 0.5	122.0 ± 2.8
Fig 6 (**d**) – eutectic lamellae (zone E)	9.7 ± 0.7	109.3 ± 2.6